

# Liquid crystal lens with corrected wavefront asymmetry

LOUIS BEGEL<sup>1</sup> AND TIGRAN GALSTIAN<sup>1,2,\*</sup>

<sup>1</sup>Center for Optics, Photonics and Lasers, Department of Physics, Engineering Physics and Optics, Université Laval, 2375 Rue de la Terrasse, Québec, Québec G1V 0A6, Canada

<sup>2</sup>Lensvector Inc. and TLCL Optical Research Inc., 6203 San Ignacio Ave. Suite 110, San Jose, California 95119, USA

\*Corresponding author: galstian@phy.ulaval.ca

Received 25 April 2018; revised 18 May 2018; accepted 22 May 2018; posted 30 May 2018 (Doc. ID 330379); published 14 June 2018

**We propose a simple technique allowing the correction of the inherent wavefront asymmetry in electrically variable liquid crystal lenses with relatively small diameters. This is achieved by splitting the peripheral hole patterned electrode of the lens in the direction of the ground-state anisotropy axis. Optical aberrations are measured before and after the split. It is demonstrated that a significant correction is achieved with a trade-off of trefoil increase in the direction of the split. This increase is then eliminated by the further segmentation of the peripheral electrode.** © 2018 Optical Society of America

**OCIS codes:** (250.0250) Optoelectronics; (080.1010) Aberrations (global); (080.3630) Lenses; (110.1085) Adaptive imaging; (160.3710) Liquid crystals.

<https://doi.org/10.1364/AO.57.005072>

## 1. INTRODUCTION

Electrically tunable liquid crystal (LC) lenses (TLCLs) have been explored over several decades [1–5] and recently have found applications in consumer electronic products (e.g., in mobile phone cameras, by Karbonn, or in webcams, by Creative) [6–10]. Those are applications requiring millimetric clear apertures (CAs), typically of the order of  $CA \approx 2$  mm. Presently their potential in ophthalmic [7,11–13] and augmented/virtual reality applications [14,15] (requiring larger CA,  $CA \geq 3$  mm) is being actively investigated. Another very important emerging area of their application is the microscopy and endoscopy (e.g., for brain study in freely behaving small animals), where, in contrary, smaller CAs are needed (typically of the order of  $CA = 0.5$  mm) [16–20]. However, in this case, the inherent asymmetric nature of TLCLs generates a significant wavefront asymmetry (“focus tilt”) and corresponding degradation of the image quality. This problem can be illustrated [Fig. 1(a)] by using one of the most promising approaches (to build TLCLs) where an LC layer (of thickness  $L$ ) is sandwiched between a hole patterned electrode (HPE) and a uniform transparent electrode [1,3,21–24]. A thin weakly conductive layer (WCL, with approximately  $10 \text{ M}\Omega/\text{sq}$  of sheet resistance) is also frequently used to soften the profile of the electric field along the  $x$  axis [6,21,23] if the aspect ratio of the lens is large,  $CA/L \gg 2.5$  [25]; see the corresponding details in the experimental section. The electric field inside of the LC layer [Fig. 1(a)] being stronger in the periphery ( $x = \pm CA/2$ ) of such a structure (compared to its center  $x = 0$ ), the molecular

reorientation (from its planar oriented ground state) is stronger in those areas. This, in turn, reduces the local effective refractive index of the material generating thus a gradient index lens.

However, this approach has an inherent problem of symmetry. Namely, the electric field’s orientation is almost symmetric in such a lens design [shown by two small diverging arrows in the center of Fig. 1(a)]. In addition, the local average molecular orientation (the so-called *director* [26]) of the LC is initially (in the ground state) aligned almost parallel to cell substrates (see hereafter). This generates dielectric torque [27] in two opposed directions that results in a spatially abrupt change of molecular orientation (so called *disclination*) that acts like an optical defect [28–30].

To avoid the appearance of this defect, various approaches have been proposed, ranging from the polymer stabilization [29], addition of two actively controlled electrodes [30], or the use of a dynamic frequency control technique, in the case if a WCL is present in the lens [6,31].

In almost all cases, however, a small ground-state tilt (so-called *pretilt*) angle  $\alpha$  is required (typically a few degrees) with respect to cell substrates to insure some minimal degree of asymmetry of the design; see Fig. 1(a). This angle is obtained by unidirectional rubbing of the thin alignment layer (typically made of polyimide, PI) of the top substrate in the “+ $x$ ” direction, while the similar layer of the bottom substrate is rubbed in the “− $x$ ” direction [shown by dashed horizontal arrows; see Fig. 1(a)]. This pretilt angle and one of the above-mentioned techniques, allow breaking the symmetry of the design and the

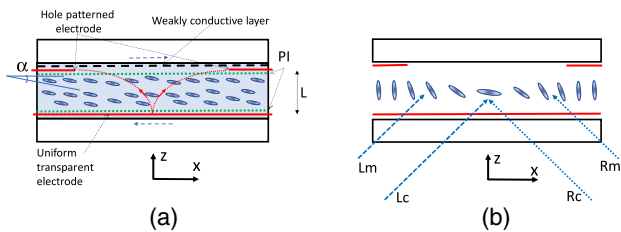


**Fig. 1.** Schematic demonstration of the TLCL using a uniform layer of LC that is sandwiched between two substrates having a hole patterned electrode and a uniform transparent electrode. (a) Ellipses show the local average molecular orientation direction;  $\alpha$  is the pretilt angle; dotted horizontal lines show the PI alignment layers. The dashed line shows the WCL. The small central arrows show the orientation of the electric field. Two dashed arrows (on substrates) show the opposed directions of the PI rubbing. (b) Schematic illustration of the origin of the asymmetry of the wavefront of light crossing the LC layer at different incidence angles (see the main text for details). The WCL and PI layers are not shown here for the sake of simplicity.

initiation of molecular reorientation in the same direction over the entire CA of the lens [Fig. 1(b)], preventing thus the appearance of disclinations.

For large values of CA, this solution (breaking the symmetry) is working rather well [3]. However, the same asymmetry is at the origin of a rather significant problem of wavefront asymmetry for lenses with smaller CA. This is particularly grave for high values of optical powers (OPs), typically used in endoscopy applications. Indeed, Fig. 1(b) demonstrates schematically this problem. It is obvious that parallel rays ( $L_m$  and  $L_c$ ), incident from the left, will not see the same refractive index profile (along the  $x$  axis) as the rays ( $R_m$  and  $R_c$ ), incident from the right. Namely, while the central rays, incident from left and right (denoted as  $L_c$  and  $R_c$ , respectively), will experience approximately the same phase delay (when crossing the LC layer), this will not be the case for middle left and middle right rays (denoted as  $L_m$  and  $R_m$ , respectively). At the exit of the LC layer, the wavefront of light will be differently tilted for the zones  $x > 0$  and  $x < 0$ , creating thus a coma. This phenomenon is experimentally demonstrated in Fig. 2 where the TLCL is placed between two crossed polarizers with the ground-state

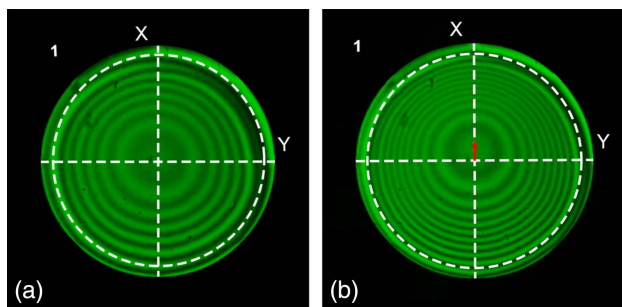


**Fig. 2.** Demonstration of the wavefront asymmetry by using the polarimetric images of the traditional TLCL with single segment HPE for (a) low ( $OP \approx 87$  D) and (b) medium ( $OP \approx 131$  D) values of OP. Red small arrow [in (b)] shows the direction of the shift that is parallel to the rubbing direction  $x$ .

director of the LC (rubbing direction  $x$ ) being aligned along the diagonal (at  $45^\circ$ ).

The technique of corresponding analyses will be presented in more details hereafter, but, in a few words, the relative phase delay between the ordinary and extraordinary polarization modes generates various polarization states at the output of the LC layer (at different radial positions  $x$ ), which are visualized as concentric (bright and dark) rings by using a green quasi-monochromatic light illumination [Fig. 2(a)]. The number of rings represents the magnitude of the generated refractive index gradient and the corresponding value of OP (see hereafter). As we can see [Fig. 2(a)], at low values of OP, the observed pattern looks more or less symmetric. However, the asymmetry becomes already visible for quite moderate values of OP [Fig. 2(b)]. Indeed, the center of the image is shifted in the direction of rubbing (shown by the small arrow in the center) as well as the distances between rings are not the same in the upper and lower parts of the pattern [Fig. 2(b)]. This confirms that the slopes of the generated wavefront are not the same on both sides of the geometric center of the TLCL since the same phase steps (e.g.,  $2\pi$ , identified by bright lines) are accumulated on noticeably larger distances when we observe it from the bottom to the center versus from the top to the same center [see also Fig. 1(b)]. It might be useful to mention that this asymmetry grows with voltage, and for much larger voltages, the wavefront becomes severely deformed in general.

A relatively complex approach was suggested to solve the above-mentioned disclination and wavefront asymmetry problems where the original LC layer (of thickness  $L$ ) is split in two parallel LC layers (of thicknesses  $L/2$ ), each layer having a ground-state molecular orientation in the same plane (perpendicular to substrates), but with opposite pretilt angles (e.g.,  $\alpha_1 = +3^\circ$  for the top layer and  $\alpha_2 = -3^\circ$  for the bottom layer) [32]. This approach can indeed eliminate the asymmetry of the wavefront and, in addition, can also increase the speed of the lens. However, its fabrication is more complex since it is more than doubling the manufacturing steps.

In the same time, a possible segmentation of the HPE (from one into four or eight segments, Fig. 3) was suggested to achieve transversal movements of the focal spot [33,34] (its low-voltage version was proposed later for optical image stabilization applications [35,36]). Another work (considering much larger lenses with  $CA = 7$  mm) was dedicated to the formation of asymmetric (or anamorphic) lenses [37]. However, none of them has discussed the problem of focus tilt (at those values of CA that tilt is negligible) neither has characterized all involved aberrations.

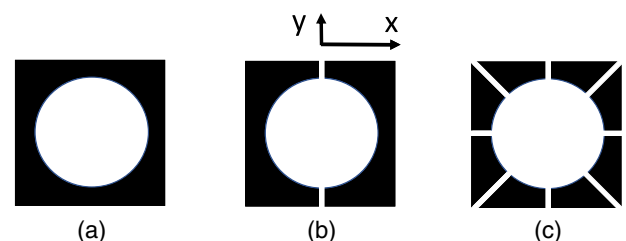


**Fig. 3.** Schematic demonstration of the TLCL's HPEs with (a) single, (b) two, and (c) eight segments.

We think that the electrode splitting approach is very promising, including for the above-mentioned asymmetry correction. However, the simple split of the HPE into only two segments [Fig. 3(b)] should be sufficient to solve the wavefront asymmetry problem, limiting thus the number of controlled electrodes to three (instead of five or more). Moreover, as we shall show below, the same (segmentation) approach can be used also to further improve the optical quality of the lens.

This work describes our experimental results demonstrating the above-mentioned wavefront asymmetry correction by using the segmentation of the peripheral electrode. We think that our approach (to reduce the wavefront asymmetry) is extremely simple from the manufacturing point of view (no additional steps are needed) and it can reduce the requirements of the relatively high pretilt angles (needed to avoid disclinations).

## 2. PROPOSED SOLUTION

### A. Experimental Conditions and Procedures

We have started our experiments by using the traditional “modal control” lens approach [21,22] to produce our lenses [Fig. 1(a)]. The CA was 0.5 mm and the diameter of the HPE was  $R = 0.55$  mm. The optical birefringence of the used home-made nematic LC mixture (HM-NLC-2C) was  $\Delta n \approx 0.219$  and the thickness  $L$  of the planar aligned LC (by using polyimide layers from Nissan) was  $59 \pm 2$   $\mu\text{m}$  (with a pretilt angle of  $\alpha \approx 3^\circ$ ). The sandwich was fabricated by using two glass substrates of 100  $\mu\text{m}$  thickness. The bottom substrate was first coated by a uniform ITO electrode and then by a PI layer. The top substrate was first coated by the WCL (see below) and then by a chrome conductive layer of 100 nm thickness. This layer was further etched into a HPE with one, two, or eight segments (Fig. 3) (with 35  $\mu\text{m}$  space between segmented electrodes). Then we spin coat the PI layer. Two PI layers obtained are then rubbed in antiparallel directions. It is important to mention that only one (the same) etching step is required to produce the HPE, no matter if it has one [Fig. 3(a)], two [Fig. 3(b)], or more [e.g., eight, Fig. 3(c)] segments. The difference between these options is the number of their electric connections (affecting the manufacturing cost) and driving schemes (affecting the cost of the driver).

We have coated the top substrate (with HPE) by a WCL since we have  $CA/L = 8.3$ . The WCL was fabricated by using a proprietary vacuum deposition technique [8] with a sheet resistivity of  $R_s \approx 40$   $\text{M}\Omega/\text{sq}$ . As we have mentioned above, this layer helps to soften the profile of the electric field as well as allows the disclination-free fast operation [6]. Namely, for a low frequency of driving signal ( $f \approx 50$  Hz, AC, square shaped) and for a sufficiently high voltage value ( $V_{\text{RMS}} \geq 3$  V), the electric field is relatively uniform in the LC layer (along the  $x$  axis) and its molecules start to be reoriented everywhere in the same direction (in the plane that is perpendicular to cell substrates). In contrast, for higher driving frequencies (e.g., at  $f \approx 5$  kHz), the electric field is noticeably reduced in the center of the cell (compared to its periphery). This generates a gradient of the refractive index and, consequently, higher values of OP. Thus, the operation of the cell can be started by applying a short low-frequency signal, followed by an

incremental increase of the frequency, to avoid the appearance of disclinations [6].

Two types of characterization techniques were applied during our experiments. The first one was the analysis of the wavefront of light (transmitted through the TLCL) by using a Shack–Hartmann wavefront sensor (from Thorlabs). The TLCL was placed in front of the sensor and a relay lens was used (between the TLCL and the sensor) to form the image of the TLCL on the entrance plane of the sensor. A polarizer was used before the TLCL to select the extraordinary polarization of the probe beam that was obtained from a CW He–Ne laser, operating at 543 nm. The diameter of the laser beam (with Gaussian transversal intensity distribution) was expanded up to 0.5 mm. That beam was incident normally on the TLCL, which was placed just behind a diaphragm of the same diameter.

Our experimental procedure was as follows. The reference wavefront was recorded without the TLCLs. Then we have introduced the TLCL and aligned its position ( $x$ ,  $y$ , and  $z$ ) by using micrometric tables. For a given voltage and frequency (applied to the TLCL), the aberrations of the lens were measured and analyzed (using Zernike coefficients). We think that, given the flat character of our lens, we should have various types of aberrations, including some degree of field curvature. The measurement of this curvature may be useful when we shall incorporate our lens with a complete optical imaging system. Since the goal of our current work is the characterization of the lens alone, we shall further measure and discuss only aberrations of order 0 to 4, according to Zernike classification, these first-order aberrations being responsible for the main deformations of the wavefront [38].

The second characterization technique consisted of using a polarimetric setup, where the TLCL sandwich was placed between two crossed polarizers with the ground-state director being oriented along the diagonal (at  $45^\circ$ ). Given that the total possible phase delay in an LC layer of thickness  $L$  and of birefringence  $\Delta n \equiv n_{\parallel} - n_{\perp}$  (where  $n_{\parallel}$  and  $n_{\perp}$  are the extraordinary and ordinary refractive indices, respectively) may be estimated as

$$\Delta\phi = (2\pi/\lambda_0)\Delta nL, \quad (1)$$

(where  $\lambda_0$  is the probe wavelength in vacuum) as well as the OP of a flat gradient index lens (with parabolic profile) is expressed (in diopters; see, e.g., in [3]) as

$$\text{OP} = 8\Delta nL/CA^2, \quad (2)$$

then the OP of the lens may be roughly estimated by the number  $N$  of observed bright or dark rings (with  $N \approx \Delta\phi/2\pi$ ) as

$$\text{OP} = 8N\lambda_0/CA^2. \quad (3)$$

Equation (3) was used for fast estimations of the OP values by using the number of observed bright and dark lines (rings) in the transmitted light (Fig. 2).

### B. Experimental Results

The modal control TLCL with single-segment HPE [Fig. 3(a)] was characterized first. Square-shaped AC voltage (4 V) was applied to the electrode with a progressive increase of its frequency from 0.5 to 11 kHz. Figure 4 shows the value of OP (■: left vertical axis, in diopters) that grows gradually



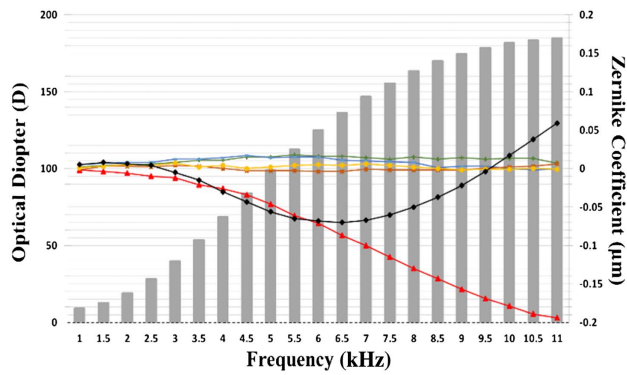


**Fig. 4.** Optical power and aberrations versus the drive frequency for the TLCL using single-segment HPE. ■: optical power, Z4 (astigmatism at  $45^\circ$ – $45^\circ$ , +), Z6 (astigmatism at  $0^\circ$ /90°, +), Z8 (coma along the  $y$  axis, +), Z9 (coma along the rubbing direction,  $x$  axis, +), Z10 (trefoil along the  $y$  axis, +), Z13 (spherical aberration, +).

and tends to saturation above  $f \approx 9$  kHz (we count  $N \approx 11$  at  $f \approx 11$  kHz). By using Eq. (3), we can estimate the obtained OP as  $\approx 160$  D that is close to the value ( $OP \approx 185$  D) obtained by the Shack–Hartman sensor. It is well known that the OP, calculated from Eq. (2), must use a value of  $\Delta n_{\text{eff}}$  (the effective birefringence of the layer) that is noticeably lower than  $\Delta n$  (since the orientation of the director is not uniform along the  $z$  axis, as well as the gradient of the refractive index along the  $x$  axis is never perfect). Interestingly enough, our observations show that, in the current TLCL, we are using almost half of the theoretically possible value ( $\approx 347$  D), which is rather low. However, we shall not investigate this question here since our main goal is the correction of the wavefront asymmetry.

Figure 4 shows also (right vertical axis in micrometers) Zernike's coefficients [39] that are responsible for the wavefront deformation. Namely, we can see different types of optical aberrations (Zernike coefficients), such as Z4 (astigmatism at  $45^\circ$ – $45^\circ$ , +), Z6 (astigmatism at  $0^\circ$ /90°, +), Z8 (coma along the  $y$  axis, +), Z9 (coma along the rubbing direction,  $x$  axis, +), Z10 (trefoil along the  $y$  axis, +), Z13 (spherical aberration, +).

**Table 1.** Values of Applied (on Two Top Semicircular Electrode Segments) Voltages and Frequencies

Frequency (kHz)	Electrode 1 (V)	Electrode 2 (V)
0.5–1	3.6	4
1.5–2–2.5–3–3.5	4.2	
4–4.5	4.3	
5	4.4	
5.5		3.9
6		3.8
6.5		3.7
7	4.4	3.6
7.5	4.5	
8	4.6	
8.5–9	4.7	3.4
9.5	4.9	3.2
10	5	3.1
10.5	5.1	2.9
11	5.2	2.8

$x$  axis, +), Z10 (trefoil along the  $y$  axis, +), and Z13 (spherical aberration, +).

As we can see, the majority of those aberrations are maintained at relatively low levels for the entire dynamic range of the OP variation. In contrast, the absolute value of coma Z9 (red triangles, responsible for the wavefront asymmetry) continuously grows, while the absolute value of the spherical aberration Z13 (black diamonds) also first grows and then decreases. While the wavefront asymmetry and the spherical aberrations are not directly related, it is worth mentioning that the last ones represent another inherent problem of TLCLs, particularly those using WCLs. We have already demonstrated [6,24] that a significant improvement of spherical aberrations may be achieved by using a floating (non-controlled) conductive layer and an appropriate choice of driving voltages. We shall thus not investigate this question hereafter.

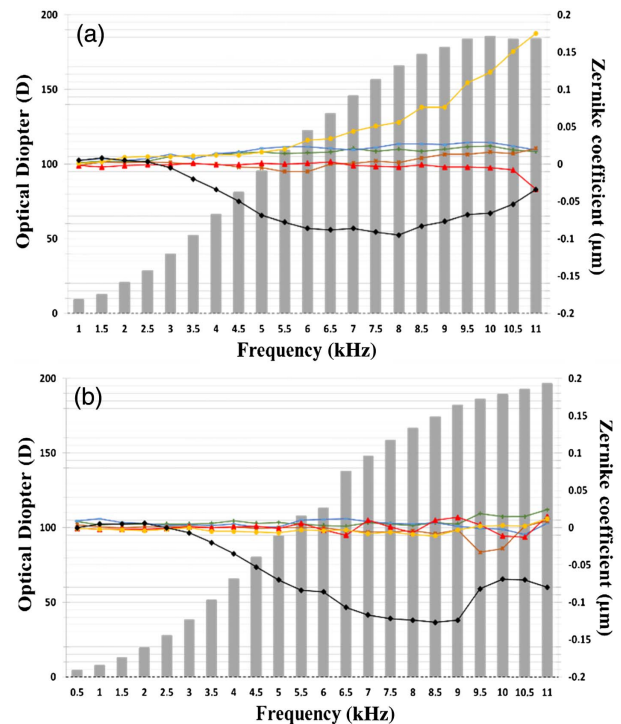


**Fig. 5.** Optical power and aberrations versus the drive frequency for the lens with HPE of (a) two segments and (b) eight segments. (c) The polarimetric image of the TLCL using eight-segment HPE at low (left) and medium (right) OP values. ■: optical power, Z4 (astigmatism at  $45^\circ$ – $45^\circ$ , +), Z6 (astigmatism at  $0^\circ$ /90°, +), Z8 (coma along the  $y$  axis, +), Z9 (coma along the rubbing direction,  $x$  axis, +), Z10 (trefoil along the  $y$  axis, +), Z13 (spherical aberration, +).

As we can see [Figs. 2(a) and 4], the asymmetry becomes quite noticeable [the center of the polarimetric pattern shifts in the rubbing direction  $x$ , Fig. 2(b)] when we increase the value of OP. By the way, to avoid higher levels of light scattering, slower response times and higher aberrations, we typically recommend using only the dynamic range of OP that is at least 15% below the maximal value of OP, that is, here, for driving (working) frequency values  $f_w \leq 8$  kHz (Fig. 4). Hereafter, we shall use this level of OP for comparisons of various aberration levels (for different lenses).

As proposed in this work, we have also fabricated TLCLs having their HPE split into two electrodes in the direction of rubbing [Fig. 3(b)]. By using this TLCL, we first tried to correct the coma (Z9). Thus, for each frequency (or OP's value), we have adjusted the voltage ratio between the two electrode segments. The optimized values of applied (on those two segments) voltages and frequencies are shown in Table 1. As we can see, the more we increase the frequency, the more the asymmetry is increasing. Thus, a larger difference of voltages (between two segments) is required to compensate that asymmetry (while still remaining far from the saturation voltages where severe deformations of wavefront are formed).

This allowed us to dramatically reduce the coma Z9 [by a factor of  $\geq 38$  for driving frequency values  $f_w \leq 7.5$  kHz, Fig. 5(a)] while keeping most of other aberrations at relatively low levels. However, there is a noticeable increase (by a factor of 25) of the trefoil aberration Z10 [yellow circles, Fig. 5(a)] and also a relatively small increase (by a factor of 1.5) of the absolute value of spherical aberration Z13. Despite those increases, the obtained performance is much better compared to the case of the single-segment HPE. However, if the above-mentioned increase (of Z10 and of Z13) might be an issue for a specific application, then either the operation of the TLCL may be limited to lower OP values (e.g., below 130 D)

or a further segmentation of the HPE may be used [Fig. 3(c)] within the same single-etching step.

We have indeed fabricated such TLCLs [with eight-segment HPE, Fig. 3(c)] to explore the potential of such an approach. As we can see from Fig. 5(b), with this lens, the trefoil aberration also can be almost eliminated (reduced by a factor of  $\geq 6$  at  $f_w \approx 8$  kHz) compared to the two-segment HPE. We are able to bring it back to the same order of magnitude as for the single-segment HPE (0.009  $\mu\text{m}$  versus 0.002  $\mu\text{m}$ ). All other aberrations also are at very low levels and the coma is well below the value we had with the single HPE lens. This was done by adjusting the voltage and frequency values applied to each segment (shown in Table 2). Figure 5(c) qualitatively demonstrates (right picture) the obtained symmetry of the wavefront for a moderate value of OP.

As it can be noticed (from Table 2), there is no an apparent symmetry for the applied voltage values. Indeed, would the material be an isotropic liquid, we would expect to have some kind of symmetry. However, the liquid crystal is an anisotropy material, aligned with a pretilt angle and the reorientation of its director is subject of the electric field, but also to elastic forces. The director may follow a different direction (then the one imposed by the electric field) to minimize the total energy of orientational deformation. Thus, the role of the segmented electrodes is not the same depending upon their position with respect to the rubbing direction and thus we do not see a symmetry. However, if two lenses have the same parameters (liquid crystal thickness, sheet resistance of the WCL, etc.), then the set of signals (to apply for the desired correction) should be the same.

Figure 6(a) presents the phase retardation distribution along the  $x$  direction, in order to compare the optical axis' shift before and after the aberration correction. Furthermore, to exhibit the evolution of RMS wavefront aberrations in all

**Table 2. Values of Applied (on Eight Segments of the Top Electrode) Voltages and Frequencies**

Frequency (kHz)	Electrode 1 (V)	Electrode 2 (V)	Electrode 3 (V)	Electrode 4 (V)	Electrode 5 (V)	Electrode 6 (V)	Electrode 7 (V)	Electrode 8 (V)
1		4.25	4.4	4.2		4.05	4.4	4.2
1.5								
2								
2.5								
3								
3.5								
4								
4.5								
5								
5.5		4.3		4.1		4	4.3	
6								
6.5								
7		4.3				3.9		4.3
7.5								
8								
8.5		4.7	4.6			3.8	4.3	4.4
9		4.8	4.7	4		3.7	4.2	4.5
9.5			4.9	3.8	3.1	3.5	3.8	4.1
10								
10.5	4.9	4.8	4.6	3.9	3.5	3.2		4.5
11	5.5	5.6	5	3.7	3.1	3	3.6	4.9

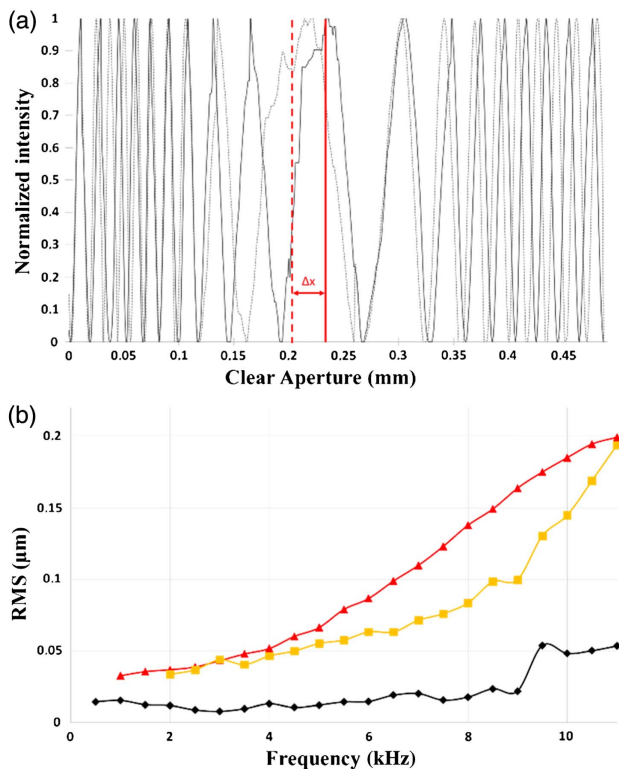


**Fig. 6.** (a) The phase retardation distribution (at 8 kHz) along the  $x$  axis. Correction of the wavefront tilt ( $\Delta x$ ) before (dashed) and after (solid) the aberration correction. (b) Optical aberrations versus the drive frequency for the case of a single electrode (triangles), two segments (square), and eight segments (diamonds), excluding the defocus (Zernike coefficient  $Z_5$ ) and third-order spherical aberrations (Zernike coefficient  $Z_{13}$ ).

above-mentioned cases, Fig. 6(b) demonstrates the magnitudes of those aberrations for various excitation frequencies in the case of a single electrode (triangles), two segments (squares), and eight segments (diamonds), excluding the defocus (Zernike coefficient  $Z_5$ ) and third-order spherical aberrations (Zernike coefficient  $Z_{13}$ ). For similar driving conditions (at 8 kHz), exposed in Fig. 2(b) (before correction) and in Fig. 5(c) (after correction), we can see that the wavefront center is corrected by approximately  $20\ \mu\text{m}$  [Fig. 6(a)]. Finally, to compare the RMS values before and after the correction (still at 8 kHz), we can see [Fig. 6(b)] that we have reached a rather significant correction factor of  $0.137/0.017 \approx 8.1$ .

### 3. CONCLUSIONS

We have demonstrated experimentally a simple technique (splitting the peripheral hole patterned electrode into segments) that enables the compensation of the wavefront asymmetry in liquid crystal lenses. This technique can be particularly important for applications requiring relatively small clear apertures. In addition, in those cases (e.g., for aspect ratio  $CA/L \approx 2.5$ ), there is no need of using WCL and thus we cannot use the frequency modulation technique to avoid the appearance of disclinations. Thus, the splitting of the HPE will also allow the operation of the lens without the appearance of disclinations.

**Funding.** Canada Research Chairs.

**Acknowledgment.** This research was supported by the Canada Research Chair in Liquid Crystals and Behavioral Biophotonics held by T. Galstian who also received the Manning Innovation Award in 2014. We would like also to thank LensVector for providing the WCL, their home-made LC mixture, and supporting us by their advice.

### REFERENCES

- S. Sato, "Applications of liquid crystals to variable-focusing lenses," *Opt. Rev.* **6**, 471–485 (1999).
- G. Li, "Adaptive lens," *Prog. Opt.* **55**, 199–283 (2010).
- T. V. Galstian, *Smart Mini-Cameras* (CRC Press, 2013).
- Y.-H. Lin, Y.-J. Wang, and V. Reshetnyak, "Liquid crystal lenses with tunable focal length," *Liq. Cryst. Rev.* **5**, 111–143 (2017).
- S. Xu, Y. Li, Y. Liu, J. Sun, H. Ren, and S.-T. Wu, "Fast-response liquid crystal microlens," *Micromachines* **5**, 300–324 (2014).
- T. Galstian, O. Sova, K. Asatryan, V. Presniakov, A. Zohrabyan, and M. Evensen, "Optical camera with liquid crystal autofocus lens," *Opt. Express* **25**, 29945–29964 (2017).
- P. Clark, T. Galstian, K. Asatryan, V. Presniakov, A. Bagramyan, A. Tork, A. Zohrabyan, and S. Careau, "Methods and apparatus for focus improvement in multiple liquid crystal cell lenses," U.S. patent 14,777,086 (11 February 2016).
- <http://www.lensvector.com>.
- Creative Technology Ltd., "Creative Live! Cam Connect HD," <http://www.impulsegamer.com/wordpress/?p=25017>.
- Karborn, "Titanium S35 model, c.j.," <http://www.karbornmobiles.com/>.
- G. Vdovin, M. Loktev, and A. Naumov, "On the possibility of intraocular adaptive optics," *Opt. Express* **11**, 810–817 (2003).
- T. Galstian and D. Brousseau, "Inductive coil sensor for vision corrective apparatus and methods therefor," U.S. patent 14,956,145 (24 March 2016).
- H. E. Milton, P. B. Morgan, J. H. Clamp, and H. F. Gleeson, "Electronic liquid crystal contact lenses for the correction of presbyopia," *Opt. Express* **22**, 8035–8040 (2014).
- H.-S. Chen, Y. J. Wang, P. J. Chen, and Y. H. Lin, "Electrically adjustable location of a projected image in augmented reality via a liquid-crystal lens," *Opt. Express* **23**, 28154–28162 (2015).
- Y.-H. Lee, G. Tan, T. Zhan, Y. Weng, G. Liu, F. Gou, F. Peng, N.-V. Tabiryan, S. Gauza, and S.-T. Wu, "Recent progress in Pancharatnam–Berry phase optical elements and the applications for virtual/augmented realities," *Opt. Data Process. Storage* **3**, 79–88 (2017).
- S. Xin, Y.-J. Wang, H.-S. Chen, X. Xiao, Y.-H. Lin, and B. Javidi, "Extended depth-of-focus 3D micro integral imaging display using a bifocal liquid crystal lens," *Opt. Lett.* **40**, 538–541 (2015).
- C.-W. Chen, M. Cho, Y. P. Huang, and B. Javidi, "Three-dimensional imaging with axially distributed sensing using electronically controlled liquid crystal lens," *Opt. Lett.* **37**, 4125–4127 (2012).
- H.-S. Chen and Y.-H. Lin, "An endoscopic system adopting a liquid crystal lens with an electrically tunable depth-of-field," *Opt. Express* **21**, 18079–18088 (2013).
- T. Galstian, K. Asatryan, V. Presniakov, A. Bagramyan, A. Tork, A. Zohrabyan, and S. Careau, "Liquid crystal optical device with advanced electric field control capability," U.S. patent 9,833,312 (07 January 2016).
- T. Galstian, A. Saghatelian, and A. Bagramyan, "Tunable optical device, tunable liquid crystal lens assembly and imaging system using same," U.S. patent 12,542,458 (17 May 2018).
- A. F. Naumov, M. Yu. Loktev, I. R. Guralnik, and G. Vdovin, "Liquid-crystal adaptive lenses with modal control," *Opt. Lett.* **23**, 992–994 (1998).
- A. Naumov, G. D. Love, M. Yu. Loktev, and F. L. Vladimirov, "Control optimization of spherical modal liquid crystal lenses," *Opt. Express* **4**, 344–352 (1999).

23. Y. Mao, B. Wang, M. Uchida, S. Yanase, S. Takahashi, and S. Sato, "Focus tuning by liquid crystal lens in imaging system," *Appl. Opt.* **51**, 7630–7635 (2012).
24. T. Galstian, K. Asatryan, V. Presniakov, A. Zohrabyan, A. Tork, A. Bagramyan, S. Careau, M. Thiboutot, and M. Cotovanu, "High optical quality electrically variable liquid crystal lens using an additional floating electrode," *Opt. Lett.* **41**, 3265–3268 (2016).
25. S. Yanase, K. Ouchi, and S. Sato, "Molecular orientation analysis of a design concept for optical properties of liquid crystal microlenses," *Jpn. J. Appl. Phys.* **40**, 6514–6521 (2001).
26. P.-G. de Gennes and J. Prost, *The Physics of Liquid Crystals*, International Series of Monographs on Physics (Oxford University, 1995), Vol. **2**, p. 4.
27. L. M. Blinov and V. G. Chigrinov, *Electrooptic Effects in Liquid Crystal Materials* (Springer, 2012).
28. B. Wang, M. Ye, and S. Sato, "Lens of electrically controllable focal length made by a glass lens and liquid-crystal layers," *Appl. Opt.* **43**, 3420–3425 (2004).
29. C. J. Hsu and C. R. Sheu, "Preventing occurrence of disclination lines in liquid crystal lenses with a large aperture by means of polymer stabilization," *Opt. Express* **19**, 14999–15008 (2011).
30. M. Ye and S. Sato, "New method of voltage application for improving response time of a liquid crystal lens," *Mol. Cryst. Liq. Cryst.* **433**, 229–236 (2005).
31. T. Galstian, P. Clark, T.-C. Antognini, J.-J. Parker, D.-A. Proudian, T.-E. Killick, and A. Zohrabyan, "Autofocus system and method," U.S. patent 12,542,458 (18 February 2010).
32. B. Wang, M. Ye, and S. Sato, "Liquid crystal lens with stacked structure of liquid-crystal layers," *Opt. Commun.* **250**, 266–273 (2005).
33. M. Ye, B. Wang, and S. Sato, "Study of liquid crystal lens with focus movable in focal plane by wave front analysis," *Jpn. J. Appl. Phys.* **45**, 6320–6322 (2006).
34. S. Masuda, S. Takahashi, T. Nose, S. Sato, and H. Ito, "Liquid-crystal microlens with a beam-steering function," *Appl. Opt.* **36**, 4772–4778 (1997).
35. T. Galstian, V. Presniakov, K. Asatryan, and A. Zohrabyan, "Image stabilization and shifting in a liquid crystal lens," U.S. patent 13,517,189 (11 October 2012).
36. N. Fraval and F. Berier, "Liquid crystal lens auto-focus extended to optical image stabilization for wafer level camera," *Proc. SPIE* **7930**, 793009 (2011).
37. M. Ye, Y. Yokoyama, and S. Sato, "Liquid crystal anamorphic lens," *Jpn. J. Appl. Phys.* **44**, 235–236 (2005).
38. W. J. Smith, *Modern Optical Engineering* (Tata McGraw-Hill Education, 1966).
39. L. N. Thibos, X. Hong, A. Bradley, and X. Cheng, "Statistical variation of aberration structure and image quality in a normal population of healthy eyes," *J. Opt. Soc. Am. A* **19**, 2329–2348 (2002).